

Pixel-scale NIR-VIS Spectral Routers Based on 2D Mie-type Metagratings

Yifan Shao¹, Shuhan Guo¹, Rui Chen¹, Yongdi Dang¹, Yi Zhou¹, Yubo Wang¹, Junjie Zhan¹, Jiaqi Yu¹, Bing-Feng Ju² and Yungui Ma^{1*}

¹State Key Lab of Modern Optical Instrumentation, Centre for Optical and Electromagnetic Research, College of Optical Science and Engineering; International Research Center (Haining) for Advanced Photonics, Zhejiang University, Hangzhou, 310058, China

²The State Key Lab of Fluid Power Transmission and Control, School of Mechanical Engineering, Zhejiang University, Hangzhou, 310027, China

Corresponding author's E-mail: yungui@zju.edu.cn

Keywords: spectral routing, image sensors, all-dielectric metagratings, Mie scattering, electromagnetic multipole modes

Abstract

The out-of-band energy loss caused by in-built color filters significantly degrades the signal-to-noise ratio and the dynamic range of conventional image sensors, which has restricted the attempt to develop ultrahigh-density imaging devices by merely shrinking the pixel size. This issue will be more serious for security cameras which need to collect visible (VIS) light and near-infrared (NIR) photons as well. The existing solutions mostly explore complex photonic nanostructures, which are often too complicated for production. In this work, we demonstrate a pixel-scale spectral router utilizing two-dimensional (2D) Si₃N₄ Mie scattering metagratings that can spatially divide NIR (850 nm) and VIS (400-700 nm) light to different pixels at high efficiencies. It has a minimum feature size larger than 360 nm, highly promising for massive production. Compared with the traditional filter design, our router can gain ~ 42% and 30% signal enhancement for NIR and VIS band, respectively. We show that it also has good polarization insensitivity and incident angle tolerance. The NIR-VIS simultaneous imaging is inspected without any complex reconstruction algorithm. Mode analysis indicates that the multipolar scattering of our Mie-type metagratings provides the necessary degrees of freedom to spatially optimize the routing functions for broadband photons.

1. Introduction

Spectral engineering is a crucial technique in many vital optical devices and apparatuses, for example, on-chip spectrometers,^[1-3] multicolor holograms,^[4-6] achromatic metalens,^[7, 8] and hyperspectral imagers.^[9, 10] The spectral selection technique is extremely significant to color imaging systems in visible and near-infrared regimes, which is usually realized by integrating color filter arrays with photonic sensors.^[11-13] However, the energy utilization efficiency of this layout is very limited as each color filter only passes narrow-band photons with the rest totally damped out. This issue will be more serious in the pursuit of ultrahigh-density compact imaging devices due to the degraded features of the signal-to-noise ratio and the dynamic range for smaller pixels.^[12-14] Various nanophotonic spectral filters have been developed to improve the transmittance,^[15-18] but can hardly resolve the problem as they employed the same mechanism (filtering) to extract color information.

To circumvent the energy loss issue encountered by classic spectral filters, spectral routers (also called color routers) that can spatially divide light to pre-defined detecting sensors according to their wavelengths have been investigated. The color separation gratings were early proposed by Dammann in 1978 using multilevel dielectric structures to separate red (R), green (G) and blue (B) bands to +1, 0 and -1 order directions, respectively.^[19] A color separation optical element was realized experimentally based on the similar design by Layet et al. in 1999.^[20] However, the large grating period and the long propagation distance from gratings to detectors limit the pixel level integration in imaging application. Recently, plasmonic gratings and multiwavelength nanoantennas have been developed,^[21-24] inducing the color routing effect in a subwavelength scale. However, the overall energy efficiency is limited by the intrinsic loss of metals. To solve the issue, all-dielectric color splitters have been proposed, based on the conception of wavelength-dependent phase control such as utilizing nanocolumns or nanostrips.^[25, 26] In these designs, the nano-splitters only occupy a small part of one unit cell and there often exists severe crosstalk between different color channels. As a consequence, color reconstruction algorithms through a conversion matrix have to be applied to restore the color information, which is unfavorable in imaging dark scenes.^[25-27] In addition, metalens arrays can be employed to route and focus light simultaneously but generally with large pixels as they need sufficient spaces to realize the routing phase profiles.^[28-30] The spatial multiplexing method utilized in some works will sacrifice the energy utilization efficiency.^[28, 29] Inverse design algorithms have been utilized to design spectral routers with high performance.^[31-39] In order to increase degrees of freedom, the device topologies are often optimized with deep

subwavelength complicated structures, but in practice hardly implementable using the current state-of-the-art technologies, especially for visible and near-infrared regimes.^[32-36] Quite recently, Bayer-type color routers with the feature size of about 100 nm have been demonstrated using the single-layer metasurface.^[38, 39] However, their fabrication needs advanced electron beam lithography (EBL) techniques, very costive for industrial production.

In this work, we demonstrate a pixel-scale spectral router based on 2D Mie-type metagratings that is able to route NIR (850 nm) photons and VIS (400-700 nm) light to distinct pixels at high energy efficiencies. Mie scattering has long been exploited to direct light or shape wavefront, but mostly for the far-field radiation.^[40-43] Here, the multipole photonic modes of Mie scatterers are fully explored to optimize the distribution of the electromagnetic fields of broadband photons just above the pixel array. Compared with conventional NIR-VIS image sensors built with color filters (having the maximum energy efficiency of 50%), our spectral router can provide much higher spectral routing efficiencies, for example, 71.18% for NIR photons and 64.27% for VIS light. It means that over 35% signal enhancement is obtained. The router with higher efficiencies (82.12% for NIR and 67.46% for VIS, i.e. about 50% signal enhancement) by Mie scatterers with the higher aspect ratio has also been verified in the simulation. The developed spectral router is further inspected on the NIR-VIS imaging function without taking any complex reconstruction algorithm. The meta-structures developed here have relatively large feature sizes above 360 nm, very promising for massive production utilizing the mature technologies such as deep UV lithography^[44] or nanoimprinting.^[45-48] The key idea to manipulate broadband photons by tailoring mutipolar scattering of big Mie scatterers other than looking for complicated nanostructures as practiced here is believed instrumental for the development of various meta-devices for practical applications.

2. Results

2.1. Design and Simulation of the Spectral Router

Figure 1a schematically shows the conventional NIR-VIS image sensors consisting of microlenses, color filters and photodetectors, where a large amount of energy is wasted due to the selective absorption of color filters. In this work, we intend to design spectral routers with the function shown in Figure 1b. The spectral router can separate NIR and VIS light onto different pixels to obtain higher spectral routing efficiencies. Then, the routed light can be filtered by color filter arrays to reduce crosstalk between different wavelength channels. As shown in Figure 1c-d, the spectral router proposed here is based on the 2D metagratings. The

unit cell of the metagratings has a period of $4\ \mu\text{m} \times 4\ \mu\text{m}$, aligned with sixteen pixels on the detecting plane. It means that the size of each pixel is $1\ \mu\text{m} \times 1\ \mu\text{m}$, well matching the pixel size of current commercial image sensors. In each unit cell, eight Si_3N_4 square [pillarsnanopillars](#), which function as Mie scatterers, are arranged on the quartz substrate, covered by SU-8 polymer which have the similar refractive index with SiO_2 . We use the Si_3N_4 [pillarsnanopillars](#) because Si_3N_4 is nearly transparent in the visible and near-infrared bands and compatible with CMOS process technologies.^[49] The optical constants of Si_3N_4 , SiO_2 and SU-8 are shown in Figure S1 (Supporting Information). The scattered field \mathbf{E}_s after passing through the metagratings is determined by the interference of electromagnetic multipole modes supported by Mie scatterers, which strongly depend on their geometries and material composition.^[50] Therefore, we can optimize the field distributions on the detecting plane of the spectral router at different wavelengths by changing the geometries of Si_3N_4 [pillarsnanopillars](#). In order to route relatively more B (400-500 nm) light to pixel 1, 4, more G (500-600 nm) light to pixel 5, 8, 9, 12, and more R (600-700 nm) light to pixel 13, 16, [pillarsnanopillars](#) with three different widths (w_1 , w_2 , w_3) are taken into consideration.

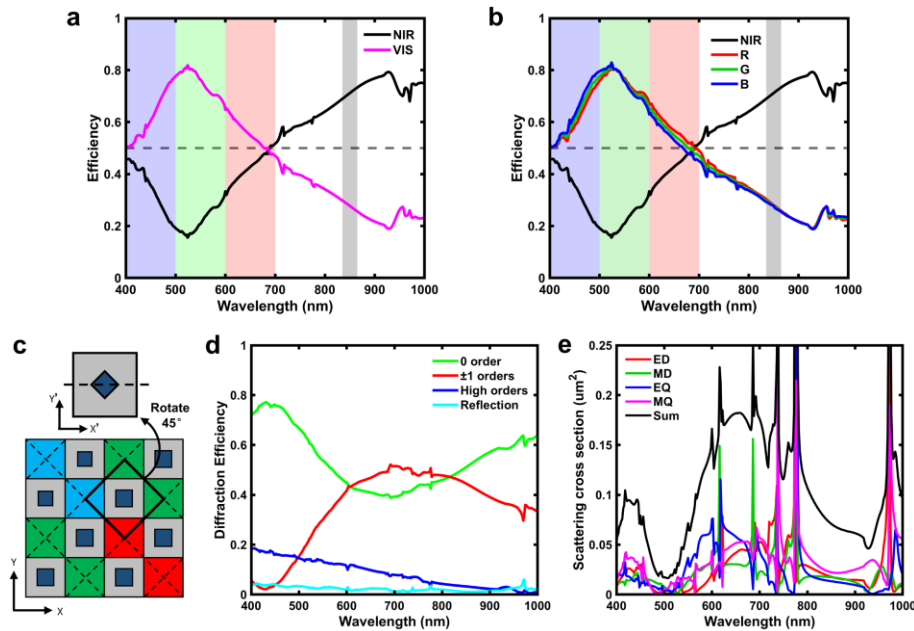
The optimization process of the spectral router is shown schematically in Figure S3 (Supporting Information). Particle swarm optimization (PSO) algorithm^[51, 52] is combined with the finite-difference time-domain numerical simulations (Lumerical FDTD Solutions) for the purpose of optimizing design parameters to obtain high spectral routing efficiency. The spectral routing efficiency at a given wavelength is defined as the ratio of the energy reaching to the corresponding detecting pixels to the total energy illuminated on the unit cell at this wavelength. Formulas to calculate spectral routing efficiency are shown in Section S2 (Supporting Information). The design parameters include widths of Si_3N_4 [pillarsnanopillars](#) (w_1 , w_2 , w_3), the height of Si_3N_4 [pillarsnanopillars](#) (h) and the distance between the detecting plane and the top of Si_3N_4 [pillarsnanopillars](#) (h_d). The figure of merit (FOM) is set to be related to spectral routing efficiencies. More details of the optimization could be found in Section S3 (Supporting Information).

After iterative optimization, final parameters are determined: $w_1 = 360\ \text{nm}$, $w_2 = 420\ \text{nm}$, $w_3 = 430\ \text{nm}$, $h = 1\ \mu\text{m}$ and $h_d = 1.4\ \mu\text{m}$. Figure 2a-d illustrate the power flow density distributions on the detecting plane (XY plane, $Z = 2.4\ \mu\text{m}$, i.e. $2.4\ \mu\text{m}$ above the substrate) of NIR (850 nm), R (630 nm), G (530 nm) and B (447 nm) light, respectively. It is obvious that NIR light is well focused on the eight pixels aligned with the Si_3N_4 [pillarsnanopillars](#) while VIS light is mainly routed to the eight pixels complementary to NIR light. Figure 2e-h shows the

power flow density distributions of the XZ cross section ($Y = 0.5 \mu\text{m}$), reflecting routing phenomena in the propagation direction at different wavelengths. The spectral routing efficiencies of NIR and VIS channels are shown in Figure 3a. The gray dashed line represents the ideal maximum spectral routing efficiency (50%) of conventional color filters utilized in NIR-VIS image sensors. The area above the dashed line and below the spectral routing efficiency curves is the total enhanced routing energy. The spectral routing efficiency of NIR (850 nm) is 71.18% while the average spectral routing efficiency of VIS band (400-700 nm) is 64.27%, with a peak efficiency of 80.36% at 530 nm.

In order to reduce crosstalk between distinct wavelength channels and extract RGB information, NIR, R, G and B filters can be arranged to corresponding pixels on the detecting plane as shown in Figure S2 (Supporting Information). The spectral routing efficiencies of NIR, R, G and B channels are shown in Figure 3b. The average spectral routing efficiencies of R (600-700 nm), G (500-600 nm) and B (400-500 nm) channels are 57.33%, 75.15% and 63.94%, respectively. G light has the best routing performance in RGB because of the location in the center of VIS band and the relatively large weight set in the optimization. Attributed to Si_3N_4 pillars/nanopillars with three distinct widths in different regions, spectral routing efficiencies of R and B channels are slightly higher (about 2%) than that of the VIS channel.

2.2. Electromagnetic Multipolar Scattering Analysis



In this section, we illustrate the physical process for the broadband light routing from the viewpoint of grating diffraction and assisted by the Mie-type scattering of nanopillar elements. To simplify the theoretical analysis, as shown in Figure 3c, the super unit-cell ($4\mu\text{m}\times 4\mu\text{m}$) for one-pixel is divided into the group of $1.14\mu\text{m}\times 1.14\mu\text{m}$ subcells profiled by the black square which have a 45° rotation angle around the z -axis. This subcell is utilized to estimate the diffraction efficiency of the periodical nanopillars and their scattering features as well. Since its size of the subcell is much larger than the largest operation wavelength, diffraction will happen and dominate the output field pattern, which is the primary reason for the spatial splitting of the colorful photons. Under this situation, the near-field coupling between the nanopillar could also be neglected. Based on these, the scattering features of nanopillar elements are manipulated through topology optimizationed to modulate the diffraction efficiency of each order and in order to then form output generate the desired interference patterns for routing at the detector plane (plane ($z = 2.4\mu\text{m}$)). Figure 3d plotted the diffraction spectral efficiency of different orders for the array of 420nm -width nanopillars calculated by a Fourier transformation for the field at the detector plane. The zero and ± 1 diffraction orders are dominant at long wavelengths ($>600\text{nm}$) while as expected, the high orders are intensified at shorter wavelengths. Controlling the relative amplitudes and phases of these orders affords the degrees of freedom to optimize the interference patterns. Here it is realized by adopting Mie-type Si_3N_4 nanopillar scatterers which have strong and wideband light interaction capabilities. To show this, as in Figure 3e, we plotted the multipolar scattering cross-section spectra of the 420nm -width nanopillars, which are calculated by decomposing (Figure 3e) the scattered field -scattering.

Mie scattering theory can be employed to explain the wavelength-dependent routing effect. Si_3N_4 pillars in 2D metagratings are performed as Mie scatterers scattering the colorful light to different regions according to their wavelengths, attributed to the dispersive behavior occurs when light interacts with matter.

After passing through nanostructures, the total electric field is $\mathbf{E} = \mathbf{E}_i + \mathbf{E}_s$, in which the incident field \mathbf{E}_i is the field that will exist in the absence of any scatterers and the scattered field \mathbf{E}_s . Besides, the scattered field \mathbf{E}_s can be expressed as the coherent superposition of field distributions of various different fundamental electromagnetic multipole modes mainly supported by Mie scatterers, including such as electric dipole (ED), magnetic dipole (MD), electric quadrupole (EQ) and magnetic quadrupole (MQ) and their summation.^[50, 53]

带格式的: 字体: 倾斜

带格式的: 字体: 倾斜

带格式的: 字体: (中文) + 中文正文 (等线), (中文) 中文 (中国)

Strong resonance could be recognized from the spectra, indicating the existence of the strong light-structure interaction. At the specific wavelength of xxx 波长 nm, the total scattering cross section is about $1.5 \mu\text{m}^2$, one third of the area ($2 \mu\text{m}^2$) of the subcell. However, like a multimode fiber, the Mie-scatterers adopted here could support multipolar modes in the wide band. As a result, the coexistence and the anti-phase features of the corresponding electric and magnetic modes give rise to very low backscattering (reflection) and relatively smooth transmission spectra as indicated in Figure 3d. In other words, the interference of the multipolar modes will majorly decide the phase of local transmitted field at the end of each nanopillar. Different

the Different multipolar contribution at different wavelengths results in the wavelength-dependent scattered field \mathbf{E}_s . In order to show existences of these modes, as shown in Figure S4 (a-b) (Supporting Information), the multipole decomposition is performed on the Si_3N_4 pillar in the Cartesian coordinates system. Because widths (w_1 , w_2 , w_3) of pillars/nanopillars are used here only a little different to slightly improve/optimize the overall efficiencies of R, G, B channels, respectively, the region framed by the black box in Figure 3e is used as the subcell (distinguished with the $4 \mu\text{m} \times 4 \mu\text{m}$ unit cell, the period of the subcell is $1.414 \mu\text{m} \times 1.414 \mu\text{m}$) to perform multipole decomposition. More details about the multipole decomposition are shown given in Section S4 (Supporting Information). The 另外理解 . Because of the dimension larger than the wavelength, the Si_3N_4 pillars/nanopillars can support several electromagnetic multipole modes that provide the necessary degrees of freedom to change the scattered field \mathbf{E}_s at different wavelengths. cElectric field distributions of in the cross section cut by indicated by the dashed line in the upper panel of Figure 3c at four different wavelengths are shown in Figure Sxx 附件 (Supporting Information)3d. From this perspective, They indicate the periodic/spatial interference of Mie scattering field with the incident field. array can routes NIR light to the center of the subcell and VIS light to four corners of the subcell. To understand the scattering feature in the super unit cell further understand the role of Mie scatterers in the routing metagrating, we also draw tThe distributions of scattered field \mathbf{E}_s and total electric field \mathbf{E} on the detecting plane at different wavelengths for one super unit-cell are shown in Figure S5-Sxx 附件 (Supporting Information). The routing effect or desired diffraction patterns for the . Because eight pillars/nanopillars are only arranged on eight NIR pixels, the incident light are mainly scattered at these regions, while the other eight VIS pixels are used to transmit the incident light directly and hardly have contribution to the scattered field. Therefore,

带格式的: 上标

带格式的: 上标

the contrast of the magnitudes of the scattered field different distribution for E_x on the detecting plane ($Z = 2.4 \mu\text{m}$) between NIR and VIS wavelengths is originating arising from the periodic interference of the optimized Mie scattering field is evidenced regions is obvious. Finally, the field distribution on the detecting plane which is the coherent superposition of incident field E_x and scattered field E_s shows the high-contrast routing performance.

2.3. Experimental Demonstration of Spectral Routing

The metagratings have been fabricated and characterized to experimentally verify the performance of NIR-VIS spectral routing. The metagratings comprised of Si_3N_4 square pillars/nanopillars are successively manufactured by plasma-enhanced chemical vapor deposition (PECVD), electron beam lithography (EBL), lift-off, reactive-ion etching (RIE) and spin coating SU-8. The fabrication process is shown in Figure S6 (Supporting Information) and Methods. Figure 4b shows the optical microscopy image of the metagratings. Figure 4c shows the top view scanning electron microscopy (SEM) image of the unit cell in the metagratings. Figure 4d is the tilted view SEM image of the unit cell. As shown in Figure 4a, the homemade microscope system is built to characterize the spectral routing effect. The sample is mounted on a nanopositioner (SmarPOD 110.45.1-SC-HV-NM, SmarACT) to ensure that the detecting plane is exactly on the focal plane of the $100\times$ objective. The spectral router is illuminated by collimated LED light beam with four different colors. Spectra of these light sources are shown in Figure S7 (Supporting Information). The pinhole and the $4f$ system are used to limit the beam size to 1 mm which is smaller than the sample in order to decrease stray light. Intensity profiles on the detecting plane are magnified and imaged onto the CMOS camera. Measured intensity profiles on the detecting plane at four different central wavelengths are shown in Figure 4e-h, in accordance with the simulation results in Figure 2a-d that produces complementary routing effect between NIR and VIS light. The spectral routing efficiencies of NIR (850 nm), R (630 nm), G (530 nm) and B (447 nm) channels are 65.15%, 60.04%, 66.22% and 60.42%, respectively. The relative efficiencies of these four wavelengths are 71.02%, 67.44%, 72.3% and 66.02%, respectively, which is defined by the ratio of the energy reaching the corresponding detecting pixels to the energy passing through the unit cell at corresponding wavelengths.

2.4. NIR-VIS Imaging with the Spectral Router

After verifying the NIR-VIS routing function, we will try the spectral router for NIR-VIS imaging. To illustrate the idea and also because of the technical limitations, we did not integrate

the spectral router with color filter arrays. Instead, NIR (850 nm), R (630 nm), G (530 nm), B (447 nm) LEDs are used as the light source separately to mimic the condition where color filter arrays are utilized on the detecting plane. Figure 5a illustrates the experimental setup for NIR-VIS imaging. The object is a structural color sample with 2×3 color blocks having different transmission spectra. The size of each color block is $16 \mu\text{m} \times 16 \mu\text{m}$. The object is imaged onto the spectral router by a $4f$ system. As shown in Figure 5b-e, the intensity profiles of each color channel on the detecting plane are measured by a $100\times$ microscope and a CMOS camera. As shown in Figure 5f-i, images of NIR, R, G and B channels are directly reconstructed in terms of the measured spectral routing efficiencies without using a conversion matrix, which is unfavorable in imaging dark scene.^[25, 26] As a contrast, original images of NIR, R, G and B channels are obtained by the system without the spectral router (Figure 5j-m). Obviously, reconstructed images are in accordance with original images for all wavelength channels. The color imaging can be realized by combining R, G and B channels (Figure 5n-o), also showing a good accordance.

3. Discussion

The measured spectral routing efficiencies are slightly reduced compared with the simulation because of the fabrication errors (e.g. the width, height and the steepness of Si_3N_4 pillars) and the interface reflection between SU-8 and free space, which is numerically analyzed in Section S8 (Supporting Information). The spectral routing efficiencies can be further improved by coating anti-reflection films on the substrate and the SU-8 layer. Besides, as shown in Figure 3(d), there exist high-order diffractions, which is not totally captured by our $100\times$ objective (numerical aperture $\text{NA} = 0.8$) for diffraction angles larger than 53° . This leads to the reduction of information on the detecting plane and energy efficiencies in the experiment.
~~The measured spectral routing efficiencies are slightly reduced compared with the simulation because of the fabrication errors (e.g. the width, height and the steepness of Si_3N_4 pillars) and the interface reflection between SU-8 and free space, which is numerically analyzed in Section S8 (Supporting Information). The spectral routing efficiencies can be further improved by coating anti-reflection films on the substrate and the SU-8 layer. Besides, as shown in Figure S9 (Supporting Information), diffraction efficiencies of different orders of the metagrating are calculated, which show the existence of high order diffraction. The field distributions on the detecting plane are the coherent superposition of the fields of these diffraction orders because it is just $1.4 \mu\text{m}$ above the scatterers rather than the far field. However, the numerical aperture~~

(NA) of the 100 \times objective used in the experiment is 0.8, which means that some energy of high order diffraction (diffraction angle higher than 53 $^\circ$) can't be collected by the objective, leading to a bit lost of information on the detecting plane and the reduced efficiencies in the experiment.

In view of the NA of actual imaging systems, the robustness to oblique incidences is an important characteristic of spectral routers. Simulated spectral responses of the spectral router under different incident angles are shown in Figure S10 (Supporting Information). The spectral router can retain above 60% spectral routing efficiency under incident angles up to 10 $^\circ$, corresponding to the NA of 0.174 in imaging systems. As shown in Figure S11 (Supporting Information), because of the symmetry of Si₃N₄ pillarsnanopillars in the metagratings, the spectral router is also of polarization-insensitive feature, which is applicable to arbitrary polarization illumination in imaging scenes. Moreover, the spin-coated SU-8 layer can be replaced by SiO₂ for industrial production. As shown in Figure S12 (Supporting Information), because SU-8 and SiO₂ have similar refractive indexes, the spectral router will retain good performance after replacing SU-8 with SiO₂. The solid spacing layer between Si₃N₄ pillarsnanopillars and the detecting plane will allow the spectral router to be integrated with image sensors, greatly enhancing the mechanical stability. This is in contrast to previously reported spectral routers that separated colors in the free space.^[25, 30, 39] The aspect ratios of Si₃N₄ pillarsnanopillars are less than 3 and the minimum feature size is 360 nm, thus highly promising for massive production, such as based on deep UV lithography^[44] and nanoimprint techniques.^[45-48] Moreover, as shown in Section S13 (Supporting Information), the spectral routing efficiency can be further improved to 82.12% for NIR photons and 67.46% for VIS light by utilizing Si₃N₄ scatterers with the aspect ratio of 6, which means about 50% energy enhancement compared with the traditional filter design.

4. Conclusion

In conclusion, we have demonstrated a pixel-scale NIR-VIS spectral router based on 2D Si₃N₄ Mie-type metagratings. About 35% signal enhancement (compared with conventional color filter scheme) enabled by the wavelength-dependent routing effect has been applied to NIR-VIS imaging experimentally, without any complex reconstruction algorithm due to the low crosstalk. The CMOS-compatible spectral router supporting massive production provides great potentials for industrial applications, especially high-density NIR-VIS imaging in low-light scenarios. Moreover, our results indicate that all-dielectric Mie scatterers can provide the

unique degrees of freedom to manipulate light-matter interactions, which offers a new pathway for the design of novel photonic devices in particular with broadband light features.

5. Methods

5.1 Numerical Simulation

Numerical simulations in this work are performed by the commercial software Lumerical FDTD Solutions. The optical constants of Si_3N_4 , SiO_2 and SU-8 utilized in the simulation are shown in Figure S1 (Supporting Information). When simulating the 2D metagratings, the $4\text{ }\mu\text{m} \times 4\text{ }\mu\text{m}$ unit cell with eight Si_3N_4 square [pillarsnanopillars](#) covered in SU-8 is modeled. The periodic boundary condition is employed for X and Y directions while the perfect matched layer condition is employed for Z direction (the propagation direction). To calculate spectral routing efficiencies of the spectral router, sixteen $1\text{ }\mu\text{m} \times 1\text{ }\mu\text{m}$ frequency domain field and power monitors are aligned with the sixteen detecting pixels respectively and arranged a distance of h_d away from the top of Si_3N_4 [pillarsnanopillars](#). Particle swarm optimization algorithm is combined with FDTD simulation to design a NIR-VIS spectral router with high spectral routing efficiencies.

5.2 Device Fabrication

The flow chart of the fabrication is shown in Figure S6 (Supporting Information): a $1\text{ }\mu\text{m}$ -thick Si_3N_4 film is deposited on the $500\text{ }\mu\text{m}$ -thick cleaned quartz substrate by plasma-enhanced chemical vapor deposition (PECVD). A 380 nm -thick ZEP520A positron beam photoresist is then spin-coated. The structural profile of the 2D metagratings is defined by the electron beam lithography (EBL). After the photoresist is developed, a 120 nm -thick Cr layer is evaporated onto the sample by electron beam evaporation. The Cr hard mask is patterned on the Si_3N_4 film after a lift-off process. The Si_3N_4 [pillarsnanopillars](#) is fabricated by reactive-ion etching (RIE). Finally, the residual Cr mask is removed and a $2.4\text{ }\mu\text{m}$ -thick SU-8 layer is spin-coated on the sample.

Supporting Information

Supporting Information is available from the Wiley Online Library or from the authors.

Acknowledgements

The authors are grateful to the partial supports from the NSFC (62075196, 61775195 and 61875174), the NSFC of Zhejiang Province (LXZ22F050001), the National Key Research and

Development Program of China (No. 2017YFA0205700) and the Fundamental Research Funds for the Central Universities.

Data and materials availability

All data are available in the main text or the supplementary materials.

Conflict of Interest

The authors declare no financial conflicts of interest.

References

- [1] J. Bao, M. G. Bawendi, *Nature* **2015**, 523, 67-70.
- [2] G. Calafiore, A. Koshelev, S. Dhuey, A. Goltsov, P. Sasorov, S. Babin, V. Yankov, S. Cabrini, C. Peroz, *Light: Sci. Appl.* **2014**, 3, e203-e203.
- [3] Z. Wang, S. Yi, A. Chen, M. Zhou, T. S. Luk, A. James, J. Nogan, W. Ross, G. Joe, A. Shahsafi, K. X. Wang, M. A. Kats, Z. Yu, *Nat. Commun.* **2019**, 10, 1020.
- [4] D. Frese, B. Sain, H. Zhou, Y. Wang, L. Huang, T. Zentgraf, *Nanophotonics* **2021**, 10, 4543-4550.
- [5] W. Wan, J. Gao, X. Yang, *Adv. Opt. Mater.* **2017**, 5, 1700541.
- [6] Y.-W. Huang, W. T. Chen, W.-Y. Tsai, P. C. Wu, C.-M. Wang, G. Sun, D. P. Tsai, *Nano Lett.* **2015**, 15, 3122-3127.
- [7] S. Wang, P. C. Wu, V.-C. Su, Y.-C. Lai, M.-K. Chen, H. Y. Kuo, B. H. Chen, Y. H. Chen, T.-T. Huang, J.-H. Wang, R.-M. Lin, C.-H. Kuan, T. Li, Z. Wang, S. Zhu, D. P. Tsai, *Nature Nanotechnology* **2018**, 13, 227-232.
- [8] R. J. Lin, V.-C. Su, S. Wang, M. K. Chen, T. L. Chung, Y. H. Chen, H. Y. Kuo, J.-W. Chen, J. Chen, Y.-T. Huang, J.-H. Wang, C. H. Chu, P. C. Wu, T. Li, Z. Wang, S. Zhu, D. P. Tsai, *Nature Nanotechnology* **2019**, 14, 227-231.
- [9] F. Yesilkoy, E. R. Arvelo, Y. Jahani, M. Liu, A. Tittl, V. Cevher, Y. Kivshar, H. Altug, *Nat. Photonics* **2019**, 13, 390-396.
- [10] D. Bannon, *Nat. Photonics* **2009**, 3, 627-629.
- [11] B. E. Bayer, *U. S. Patent 3971065*, **1976**.
- [12] Y. Huo, C. C. Fesenmaier, P. B. Catrysse, *Opt. Express* **2010**, 18, 5861-5872.
- [13] H. Abe, in *Proc. IEDM* **2004**, 989-992.
- [14] A. Theuwissen, in *Proc. 33rd ESSCIRC* **2007**, 21-27.

- [15] J. Berzinš, S. Fasold, T. Pertsch, S. M. B. Bäumer, F. Setzpfandt, *ACS Photonics* **2019**, *6*, 1018-1025.
- [16] A. F. Kaplan, T. Xu, L. Jay Guo, *Appl. Phys. Lett.* **2011**, *99*, 143111.
- [17] Q. Chen, D. Das, D. Chitnis, K. Walls, T. D. Drysdale, S. Collins, D. R. S. Cumming, *Plasmonics* **2012**, *7*, 695-699.
- [18] S. P. Burgos, S. Yokogawa, H. A. Atwater, *ACS Nano* **2013**, *7*, 10038-10047.
- [19] H. Dammann, *Appl. Opt.* **1978**, *17*, 2273-2279.
- [20] B. Layet, I. G. Cormack, M. R. Taghizadeh, *Appl. Opt.* **1999**, *38*, 7193-7201.
- [21] E. Laux, C. Genet, T. Skauli, T. W. Ebbesen, *Nat. Photonics* **2008**, *2*, 161-164.
- [22] S. H. Alavi Lavasani, T. Pakizeh, *J. Opt. Soc. Am. B* **2012**, *29*, 1361-1366.
- [23] T. Shegai, S. Chen, V. D. Miljković, G. Zengin, P. Johansson, M. Käll, *Nat. Commun.* **2011**, *2*, 481.
- [24] X. Zhuo, H. K. Yip, X. Cui, J. Wang, H.-Q. Lin, *Light: Sci. Appl.* **2019**, *8*, 39.
- [25] M. Miyata, M. Nakajima, T. Hashimoto, *ACS Photonics* **2019**, *6*, 1442-1450.
- [26] S. Nishiwaki, T. Nakamura, M. Hiramoto, T. Fujii, M.-a. Suzuki, *Nat. Photonics* **2013**, *7*, 240-246.
- [27] P. Wang, R. Menon, *Optica* **2015**, *2*, 933-939.
- [28] B. H. Chen, P. C. Wu, V.-C. Su, Y.-C. Lai, C. H. Chu, I. C. Lee, J.-W. Chen, Y. H. Chen, Y.-C. Lan, C.-H. Kuan, D. P. Tsai, *Nano Lett.* **2017**, *17*, 6345-6352.
- [29] D. Lin, A. L. Holsteen, E. Maguid, G. Wetzstein, P. G. Kik, E. Hasman, M. L. Brongersma, *Nano Lett.* **2016**, *16*, 7671-7676.
- [30] M. Miyata, N. Nemoto, K. Shikama, F. Kobayashi, T. Hashimoto, *Optica* **2021**, *8*, 1596-1604.
- [31] D. Sell, J. Yang, S. Doshay, J. A. Fan, *Adv. Opt. Mater.* **2017**, *5*, 1700645.
- [32] P. Camayd-Muoz, C. Ballew, G. Roberts, A. Faraon, *Optica* **2020**, *7*, 280-283.
- [33] N. Zhao, P. B. Catrysse, S. Fan, *Adv. Photon. Res.* **2021**, *2*, 2000048.
- [34] M. Chen, L. Wen, D. Pan, D. R. S. Cumming, X. Yang, Q. Chen, *Nanoscale* **2021**, *13*, 13024-13029.
- [35] E. Johlin, *iScience* **2021**, *24*, 102268.
- [36] P. B. Catrysse, N. Zhao, W. Jin, S. Fan, *Nanophotonics* **2022**, *11*, 2381-2387.
- [37] Q. Chen, X. Nan, M. Chen, D. Pan, X. Yang, L. Wen, *Adv. Mater.* **2021**, *33*, 2103815.
- [38] X. Zou, Y. Zhang, R. Lin, G. Gong, S. Wang, S. Zhu, Z. Wang, *Nat. Commun.* **2022**, *13*, 3288.

- [39] J. Li, Q. Zhang, H. Yang, T. Lei, L. Du, X. Wang, J. Bu, Q. Chen, Y. Liu, Z. Xie, X. Yuan, *ACS Photonics* **2022**, 9, 2607-2613.
- [40] J. Li, N. Verellen, D. Vercruysse, T. Bearda, L. Lagae, P. Van Dorpe, *Nano Lett.* **2016**, 16, 4396-4403.
- [41] E. Khaidarov, H. Hao, R. Paniagua-Domínguez, Y. F. Yu, Y. H. Fu, V. Valuckas, S. L. K. Yap, Y. T. Toh, J. S. K. Ng, A. I. Kuznetsov, *Nano Lett.* **2017**, 17, 6267-6272.
- [42] P. Albella, T. Shibanuma, S. A. Maier, *Scientific Reports* **2015**, 5, 18322.
- [43] T. Shibanuma, T. Matsui, T. Roschuk, J. Wojcik, P. Mascher, P. Albella, S. A. Maier, *ACS Photonics* **2017**, 4, 489-494.
- [44] M. Keil, A. E. Wetzel, K. Wu, E. Khomtchenko, J. Urbankova, A. Boisen, T. Rindzevicius, A.-I. Bunea, R. J. Taboryski, *Nanoscale Adv.* **2021**, 3, 2236-2244.
- [45] S. Zankovych, T. Hoffmann, J. Seekamp, J. U. Bruch, C. M. S. Torres, *Nanotechnology* **2001**, 12, 91-95.
- [46] S. C. Johnson, T. C. Bailey, M. D. Dickey, B. J. Smith, E. K. Kim, A. T. Jamieson, N. A. Stacey, J. G. Ekerdt, C. G. Willson, D. P. Mancini, W. J. Dauksher, K. J. Nordquist, D. J. Resnick, in *Proc. SPIE* **2003**, 5037 197-202.
- [47] S. H. Ahn, L. J. Guo, *Adv. Mater.* **2008**, 20, 2044-2049.
- [48] Q. Chen, G. Hubbard, P. A. Shields, C. Liu, D. W. E. Allsopp, W. N. Wang, S. Abbott, *Appl. Phys. Lett.* **2009**, 94, 263118.
- [49] S. Colburn, A. Zhan, E. Bayati, J. Whitehead, A. Ryou, L. Huang, A. Majumdar, *Opt. Mater. Express* **2018**, 8, 2330-2344.
- [50] P. Grahm, A. Shevchenko, M. Kaivola, *New J. Phys.* **2012**, 14, 093033.
- [51] Y. Zhang, S. Wang, G. Ji, *Math. Probl. Eng.* **2015**, 2015, 931256.
- [52] S. Pervaiz, Z. Ul-Qayyum, W. H. Bangyal, L. Gao, J. Ahmad, *Comput. Math. Method. M.* **2021**, 2021, 5990999.
- [53] R. Alaei, C. Rockstuhl, I. Fernandez-Corbaton, *Opt. Commun.* **2018**, 407, 17-21.

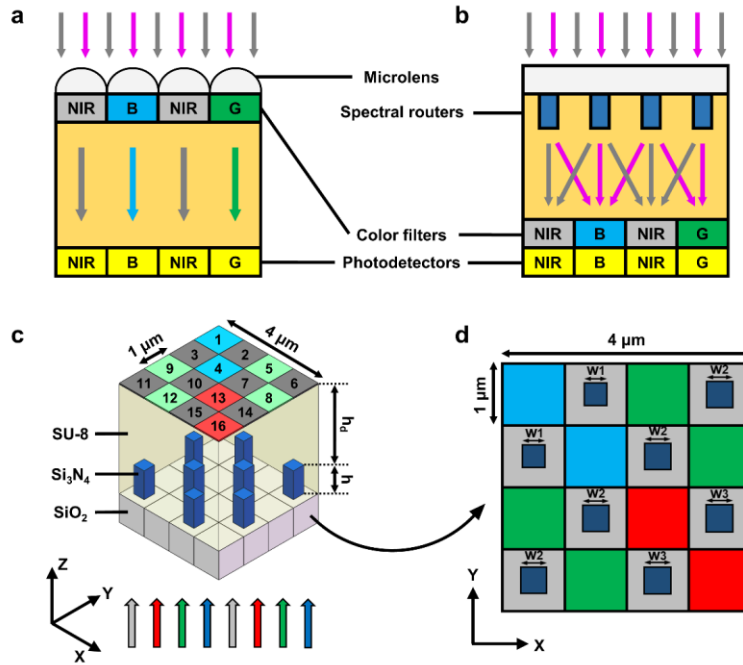


Figure 1. a) Schematic side view of the conventional NIR-VIS image sensors with color filters. b) Schematic side view of the NIR-VIS image sensors with spectral routers. Gray arrows and violet arrows in (a-b) represent NIR and VIS light respectively. c) Schematic of the spectral router with Si₃N₄ pillars covered by SU-8 on a quartz substrate, h is the height of Si₃N₄ pillars, h_d is the distance between the detecting plane and the top of Si₃N₄ pillars. d) Schematic top view of the 4 μm × 4 μm unit cell in the spectral router, including sixteen pixels. The eight gray pixels are intended to collect NIR light (850 nm) while the other eight pixels are intended to collect VIS light (400-700 nm). NIR, R, G and B color filters can be correspondingly arranged on the detecting plane to extract color information and eliminate crosstalk between color channels.

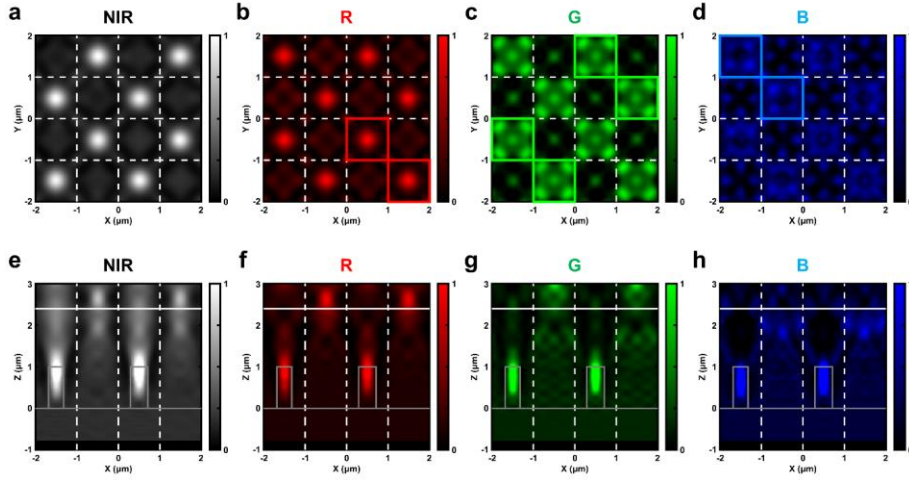
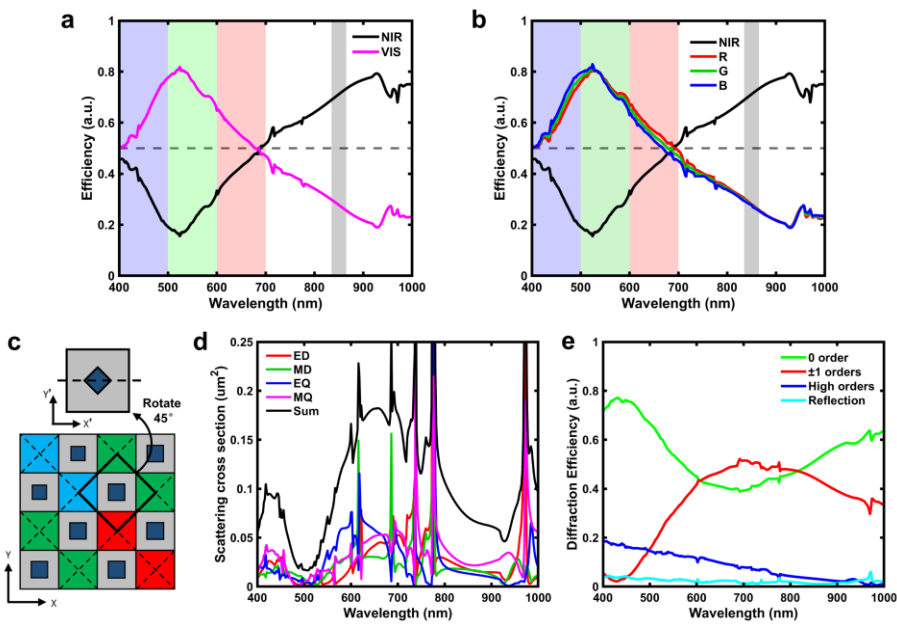
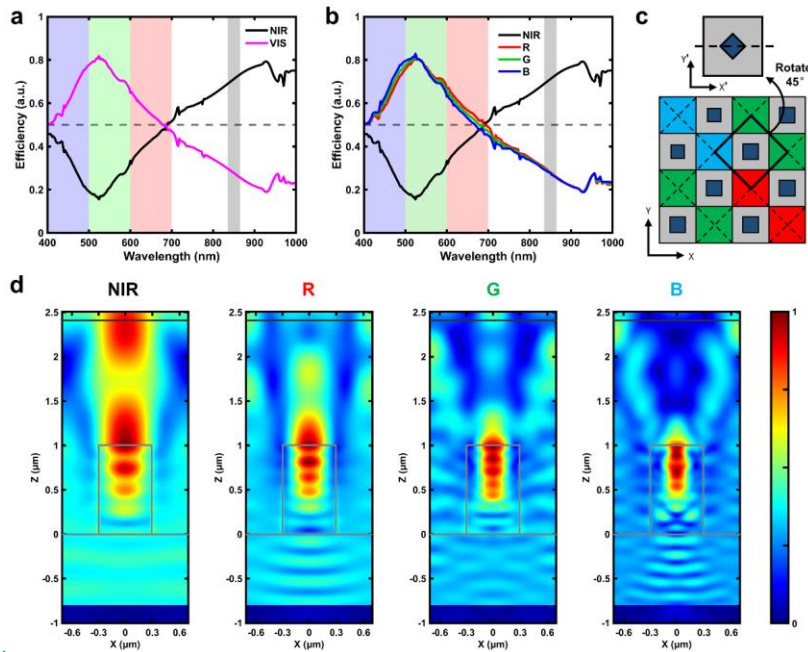


Figure 2. a-d) Simulated power flow density distributions on the detecting plane in a unit cell at wavelengths of 850 nm, 630 nm, 530 nm and 447 nm, respectively. The R, G and B boxes in (b-d) represent pixels that can be arranged with R, G and B filters, respectively, while the other eight pixels can be arranged with NIR filters. e-h) Simulated power flow density distributions of the XZ cross section ($Y = 0.5 \mu\text{m}$) at wavelengths of 850 nm, 630 nm, 530 nm and 447 nm, respectively. The coordinate system is shown in Figure 1c. Gray rectangular boxes represent Si_3N_4 pillars. The white solid line at $Z = 2.4 \mu\text{m}$ is the detecting plane.



带格式的: 字体: (中文)+中文正文 (等线)

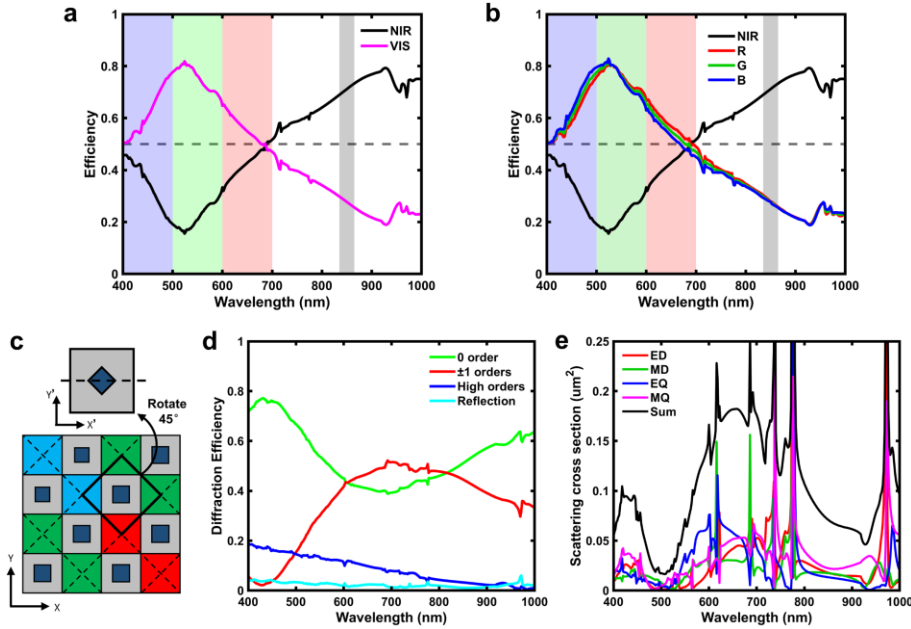


Figure 3. a) Simulated spectral routing efficiencies of NIR and VIS channels. b) Simulated spectral routing efficiencies of NIR, R, G and B channels if color filters are arranged. The horizontal dashed line in (a-b) represents the maximum spectral routing efficiency of ideal NIR and VIS filters. The gray, R, G and B strip regions in (a-b) represent the working bands of each color channel respectively. c) The region framed by the black box can be seen as regarded as the subcell of the metagrating. The coordinate system is rotated by 45°. d) Electric field distributions of the cross section cut by the dashed line in the upper panel of (e) at wavelengths of 850 nm, 630 nm, 530 nm and 447 nm, respectively. The gray rectangular box represents the Si_3N_4 pillar. The gray solid line at $Z = 2.4 \mu\text{m}$ is the detecting plane. Diffraction efficiencies of different diffraction orders of the metagrating. The ± 1 orders (red line) include the contribution of eight orders, i.e., $(0, \pm 1)$, $(\pm 1, 0)$, $(\pm 1, \pm 1)$ orders. (e) Scattering cross sections of the subunit cell with element size of 420 nm for electric dipole (ED), magnetic dipole (MD), electric quadrupole (EQ) and magnetic quadrupole (MQ). The region framed by the black box in (c) is used as the subcell for calculation in (d,e).

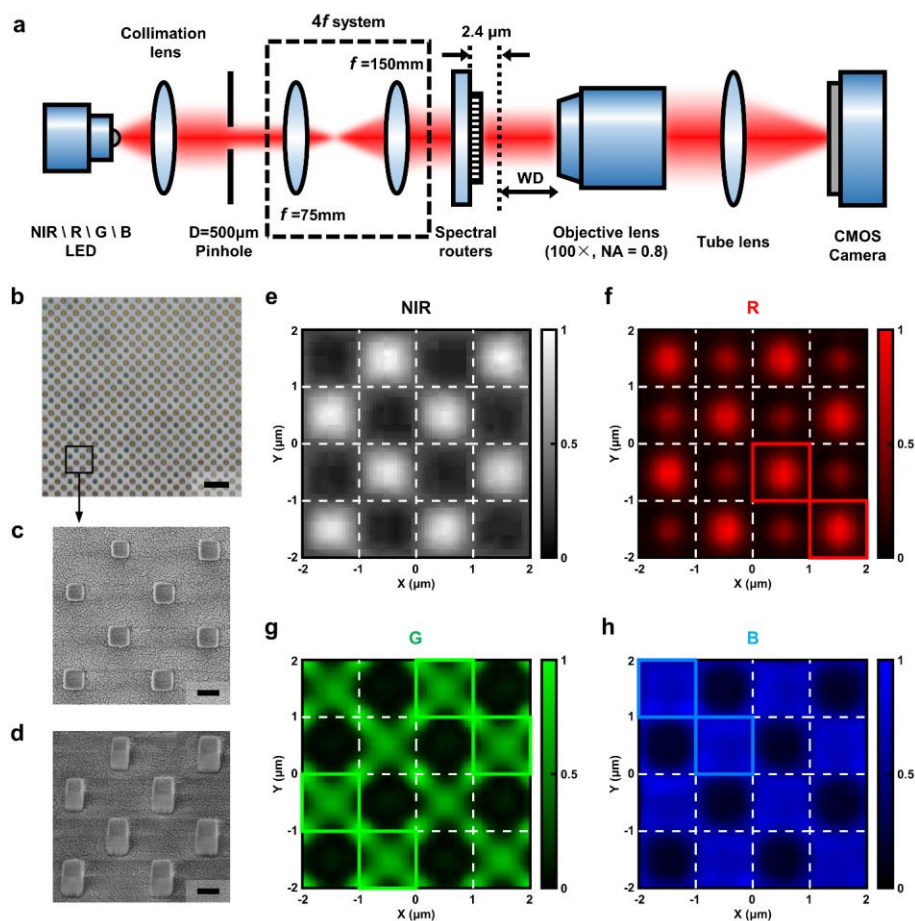


Figure 4. Experimental characterizations of the spectral router. a) Schematic of the optical measurement setup. The pinhole and the 4f system are used to limit the beam size. b) Optical microscopy image of the metagratings. Scale bar: 4 μm. c) Top view SEM image of the unit cell in the metagratings. d) Tilted view SEM image of the unit cell in the metagratings. e-h) Measured intensity profiles on the detecting plane in a unit cell at wavelengths of 850 nm, 630 nm, 530 nm and 447 nm, respectively.

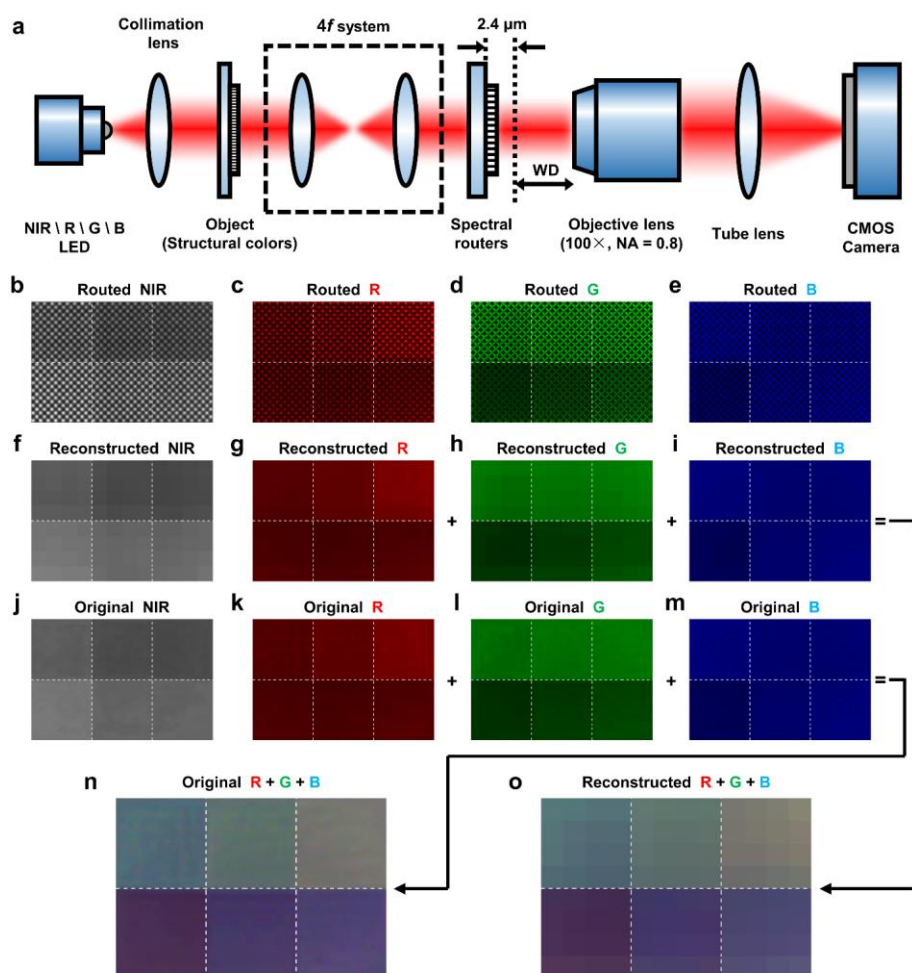


Figure 5. NIR-VIS imaging based on the spectral router. a) Schematic of the experimental setup of the NIR-VIS imaging with the spectral router. NIR, R, G and B LEDs are used as the light source one at a time respectively to mimic color filter arrays on the detecting plane. The 4f system is used to image the object (2 \times 3 color blocks) onto the spectral router. b-e) Measured intensity profiles of each color channel on the detecting plane after the image is routed. f-i) Reconstructed images of each color channel. j-m) Original images of each color channel obtained by the setup without the spectral router. n) Original color image obtained by (k)+(l)+(m). o) Reconstructed color image obtained by (g)+(h)+(i).

Table of contents

The spectral router with the feature size larger than 360nm can spatially separate NIR (850 nm) and VIS (400-700 nm) light to different pixels at high efficiencies, attributed to the optimized multipolar interference supported by Si_3N_4 Mie scatterers in the metagrating. It can replace the filter design in traditional NIR-VIS image sensors to improve the signal-to-noise ratio and the dynamic range.

Pixel-scale NIR-VIS Spectral Routers Based on 2D Mie-type Metagratings

Yifan Shao, Shuhan Guo, Rui Chen, Yongdi Dang, Yi Zhou, Yubo Wang, Junjie Zhan, Jiaqi Yu, Bing-Feng Ju and Yungui Ma*

Figure for TOC